PAPER

Check for updates

Surface-modified Ti₃C₂ MXene nanosheets for mesenchymal stem cell osteogenic differentiation *via* photothermal conversion

Jiebing Zhang, Shuang Tang, Ning Ding, Ping Ma and Zutai Zhang 📧 *

In the field of bone tissue engineering, the practical application of growth factors is limited by various factors such as systemic toxicity, instability, and the potential to induce inflammation. To circumvent these limitations, the use of physical signals, such as thermal stimulation, to regulate stem cells has been proposed as a promising alternative. The present study aims to investigate the potential of the two-dimensional nanomaterial Ti₃C₂ MXene, which exhibits unique photothermal properties, to induce osteogenic differentiation of bone marrow-derived mesenchymal stem cells (BMSCs) *via* photothermal conversion. Surface modification of Ti₃C₂ MXene nanosheets with PVP (Ti₃C₂–PVP) was employed to enhance their colloidal stability in physiological solutions. Characterization and cellular experiments showed that Ti₃C₂–PVP nanosheets have favorable photothermal properties and biocompatibility. Our study demonstrated that the induction of photothermal stimulation by co-culturing Ti₃C₂–PVP nanosheets with BMSCs and subsequent irradiation with 808 nm NIR significantly promoted cell proliferation, adhesion and osteogenic differentiation of BMSCs. In conclusion, the results of this study suggest that Ti₃C₂–PVP is a promising material for bone tissue engineering applications as it can modulate the cellular functions of BMSCs through photothermal conversion.

Introduction

Bone tissue engineering is a promising approach for treating severe bone defects because it can reduce the complications associated with autograft use, particularly those related to donor site healing.[1,2] Bone tissue engineering involves three key elements: seed cells, scaffolds, and growth factors.[3] *In vitro* cell culture on tissue engineering materials is an option, but the high cost and complex regulatory requirements of biological components have led to a preference for the recruitment of the patient's own cells from surrounding tissues.[4] Bone marrow-derived mesenchymal stem cells (BMSCs) are critical for the generation of cells such as osteoblasts, which play a critical role in maintaining bone tissue homeostasis and repairing bone defects.[5] In bone tissue engineering, the use of artificial materials requires the supplementation of growth factors such as FGF, VEGF, IGF, TGF-β, PDGF, and BMP to stimulate the differentiation of BMSCs into osteoblasts.[6,7] Although growth factors play a crucial role in bone tissue engineering, their practical application is limited by issues such as systemic toxicity, instability, and the potential to induce inflammation.[8]

The application of physical signals to regulate stem cell fate has become an area of increasing interest in the fields of biomaterials, tissue engineering, and cell biology.[9] Physical

School of Stomatology, Capital Medical University, Beijing, PR China. E-mail: zutaizhang@ccmu.edu.cn

signals offer an alternative to the use of growth factors in bone tissue engineering, by providing a safe, targeted, and adjustable method.[10] There are six categories of physical signals that can be sensed by cells, including mechanical, optical, thermal, electrical, acoustic, and magnetic.[10] Thermal stimulation, as a physical signal, is known to have both positive and negative effects on biological systems. While elevated temperatures above 46 °C have been shown to cause cell death and tissue damage,[11] mild thermal stimulation at temperatures between 40 and 42 °C, which is only 3–5 °C above the normal body temperature, has been shown to regulate stem cell differentiation and facilitate bone regeneration.[10,12–14]

Traditional direct thermal treatments, such as hot compresses, have limitations in that they primarily affect superficial areas and lack precise control over temperature and duration. To further exploit the osteogenic effects of mild thermal stimulation and overcome these limitations, researchers have employed methods to deliver heat to deep body tissues using magnetic fields, infrared radiation, and X-rays.[15] Photothermal therapy (PTT) has gained prominence in biomedicine due to its capacity to selectively convert near-infrared (NIR) light, which exhibits good transmissivity, into heat through photothermal conversion. This addresses the challenge of delivering thermal stimulation efficiently to deep, specific lesion sites within the human body.[16] PTT is primarily utilized for cancer treatment and antimicrobial therapy,[17,18] offering advantages such as the absence of drug resistance and

minimal side effects compared to conventional chemotherapy.[19]

Recent research has generated a growing interest in the utilization of two-dimensional (2D) nanomaterials, an emerging class of photothermal agents with unique physical and chemical properties, to deliver thermal stimulation in the field of bone tissue engineering.[15,20,21] Ti_3C_2 MXene is a kind of 2D nanomaterials which holds great promise due to their biocompatibility, high absorption of NIR, and efficient photothermal conversion ability.[22,23] Although some studies have suggested the potential of Ti_3C_2 MXene to promote osteogenesis in mesenchymal stem cells, the effect of photothermal modulation remains under-investigated.[24] Our hypothesis is that Ti_3C_2 MXene could be an optimal photothermal agent to deliver thermal stimulation in order to induce osteogenic differentiation of BMSCs and potentially reduce the reliance on growth factors.

The aim of this study is to investigate the photothermal modulation of BMSCs by Ti_3C_2 MXene nanosheets under NIR irradiation. To overcome the limitations of instability and oxidation susceptibility of Ti_3C_2 MXene,[25,26] poly(N-vinyl-pyrrolidone) (PVP) was used to modify the nanosheets. PVP is an amphiphilic, water-soluble polymer. Demonstrated as non-irritating to skin, eyes, and mucosa, PVP exhibits excellent tissue compatibility.[28] Owing to its remarkable solubility in various conventional solvents, low toxicity and chemical stability, the use of PVP for surface modification has been extensively explored in the field of pharmaceutical manufacturing and biomaterial development.[27] The surface-modified Ti_3C_2 (Ti_3C_2–PVP) nanosheets showed improved stability in physiological solutions, excellent biocompatibility, and enhanced osteogenic activity in cellular experiments. Furthermore, thermal stimulation generated by NIR light was found to modulate the proliferation, adhesion, and osteogenic differentiation of BMSCs. These results are expected to provide a deeper insight into the photothermal modulation of BMSCs by Ti_3C_2 MXene nanosheets under NIR irradiation and its potential applications in bone tissue engineering.

Experimental

Synthesis of Ti_3C_2 MXene nanosheets

The preparation of Ti_3C_2 MXene was performed according to the MILD method.[29] First, 0.8 g of LiF was added to 10 mL of 9 M HCl to prepare the etching solution. Next, the Ti_3AlC_2 MAX powder was slowly added to the etching solution and stirred at a constant temperature of 35 °C for 48 hours. After the reaction, the resulting product was centrifuged and washed several times with deionized water, followed by further hand shaking and centrifugation to obtain a suspension of Ti_3C_2 MXene nanosheets.

Surface modification of Ti_3C_2 MXene nanosheets (Ti_3C_2–PVP)

The process of modifying Ti_3C_2 MXene nanosheets with PVP was carried out to improve the stability. A mixture of 25 mg of Ti_3C_2 MXene and 200 mg of PVP with an average molecular weight of 40 000 was dissolved in 100 mL of ethanol. This solution was then stirred overnight at 50 °C. The final product, Ti_3C_2–PVP, was obtained by centrifugation and multiple washes with water and ethanol. Ti_3C_2 and Ti_3C_2–PVP colloidal solutions were diluted to a concentration of 25 μg mL^{-1} using deionized water, PBS, and Dulbecco's modified Eagle's medium (DMEM). The solutions were placed in vials and allowed to stand undisturbed for one week. Digital photographs were taken to observe and evaluate the stability of Ti_3C_2 and Ti_3C_2–PVP.

Characterization

The morphology of the samples was studied by scanning electron microscopy (SEM, GEMINI 300, ZEISS, Germany) and transmission electron microscopy (TEM, Talos F200x, FEI, USA). The crystal structure was analyzed by X-ray diffraction (XRD, D8A25, Bruker, Germany). UV-vis-NIR absorption spectra were recorded using a UV-vis-NIR spectrometer (UV-3600i Plus, SHIMADZU, Japan). Particle size and zeta-potential were measured using dynamic light scattering (DLS) and zeta-potential measurements on a Zetasizer Nanoseries instrument (ZS90, Malvern, UK). The photothermal properties of the samples were evaluated under 808 nm NIR light (LASERWAVE, China) and the temperature was recorded using an Infrared Thermal Imager (InfiRay, China).

Cell culture

Mouse bone marrow-derived mesenchymal stem cells (BMSCs) were obtained from Jinyuan Technology (China) and cultured in RPMI-1640 medium (Gibco, USA) that was supplemented with 10% fetal bovine serum (FBS, Gibco, USA) and 1% penicillin/streptomycin (Invitrogen, USA). Cells were maintained in a controlled environment in an incubator at 5% CO_2 and 95% relative humidity.

NIR irradiation of BMSCs

The BMSCs were co-cultured with 12.5 μg mL^{-1} of Ti_3C_2–PVP nanosheets. The control group consisted of growth medium only. The cells were exposed to exposure to an 808 nm near-infrared laser (LASERWAVE, China) until the temperature reached 42 °C and was maintained at this temperature for a duration of 5 minutes once a day.

Cell proliferation

To evaluate cell proliferation, the BMSCs were seeded and cultured overnight in 96-well plates at a density of 5000 cells per well. Ti_3C_2–PVP nanosheet colloidal solution was diluted with complete medium at concentrations of 50, 25, and 12.5 μg mL^{-1}, while the control group consisted of pure complete medium. Cell viability was evaluated at 1, 3, 5, and 7 days using the Cell Counting Kit-8 (CCK-8, Dojindo, Japan). Absorbance values were measured using a microplate reader (BioTek, USA) at a wavelength of 450 nm. The relative cell proliferation rate was calculated as (experimental OD − control OD)/control OD.

Live/dead assay

The BMSCs were seeded at a density of 10 000 cells per well in 24-well plates. Twenty-four hours after NIR irradiation, the samples were rinsed three times with PBS, incubated with calcein-AM and propidium iodide (PI) for 30 minutes at 37 °C in the dark, and observed with a fluorescence microscope (Olympus, Japan).

Cell morphology

The BMSCs were cultured in 24-well plates on 14 mm diameter coverslips at a density of 10 000 cells per well. The cell morphology was observed by phase-contrast microscopy (Olympus, Japan) for bright field imaging. For SEM observation, cells were fixed in a 2.5% glutaraldehyde solution overnight at 4 °C. After thorough rinsing with PBS three times, the samples underwent a sequential ethanol dehydration process at increasing concentrations (50%, 75%, 85%, 95%, and 100%). To visualize the cytoskeleton, the samples were washed, fixed, permeabilized, blocked, and incubated with Alexa Fluor 488-phalloidin (Invitrogen, USA) for actin staining and DAPI (Invitrogen, USA) for nuclear staining. The samples were then observed under a fluorescence microscope (Olympus, Japan). Quantification was performed by calculating the area of cell spreading (represented in green) using ImageJ software.

Quantitative reverse transcription-PCR (qRT-PCR)

The BMSCs were cultured in 12-well plates and exposed to 12.5 µg mL^{-1} Ti$_3$C$_2$–PVP nanosheets and NIR light. Osteogenesis induction medium was prepared by supplementing the complete medium with 10 nM dexamethasone, 10 mM sodium β-glycerol phosphate disodium, and 50 µg mL^{-1} ascorbic acid. After osteogenesis induction for 14 days, total RNA was extracted using Cell Total RNA Isolation Kit (Vazyme, China). Reverse transcription was performed to generate cDNA using HiScript III All-in-one RT SuperMix (Vazyme, China). Then, a 20 µL quantitative real-time PCR system was established using the Taq Pro Universal SYBR qPCR Master Mix (Vazyme, China). Real-time fluorescence quantitative PCR analysis was performed using a real-time fluorescence quantitative PCR system (Bio-Rad, USA). Relative gene expression levels were determined by the $\Delta\Delta C_t$ method and normalized by GAPDH. Primer sequences used in the analysis are listed below:

GAPDH: F-5′-AGGTCGGTGTGAACGGATTTG-3′, R-5′-TGTAGACCATGTAGTTGAGGTCA-3′;

ALP: F-5′-TCCGTGGGCATTGTGACTAC-3′, R-5′-TGGTGGCATCTCGTTATCCG-3′;

OCN: F-5′-GGTAGTGAACAGACTCCGGC-3′, R-5′-GGCGGTCTTCAAGCCATACT-3′;

OPN: F-5′-ATCTCACCATTCGGATGAGTCT-3′, R-5′-TGTAGGGACGATTGGAGTGAAA-3′;

RUNX2: F-5′-GACTGTGGTTACCGTCATGGC-3′, R-5′-ACTTGGTTTTTCATAACAGCGGA-3′;

COL1: F-5′-GCTCCTCTTAGGGGCCACT-3′, R-5′-ATTGGGGACCCTTAGGCCAT-3′.

ALP staining

The BMSCs were cultured in 12-well plates and exposed to 12.5 µg mL^{-1} Ti$_3$C$_2$–PVP nanosheets and NIR light. After 7 days of osteogenic induction, the samples were fixed in 4% para-formaldehyde for 30 minutes and rinsed with PBS. The BCIP/NBT ALP staining kit from Beyotime Biotechnology (China) was used to perform the staining procedure. The samples were incubated with the working staining solution for 24 hours at room temperature in the dark. The samples were then visualized by microscopy, and the quantification of ALP-positive areas was performed using ImageJ software. Quantification was performed by calculating the ratio of the stained area (represented in blue) to the total area (stained area/total area × 100%).

Alizarin red staining

For alizarin red staining (ARS) procedure, the BMSCs were induced under conditions similar to those employed for the ALP staining. After a period of 14 days of osteogenic induction, the cells were fixed with 4% paraformaldehyde for 30 minutes and then rinsed thoroughly with PBS without Ca^{2+} and Mg^{2+}. Subsequently, the samples were incubated with 0.1% ARS solution for 30 minutes in the dark. Calcium deposits were quantified by determining the ratio of stained area (red) to total area using ImageJ software.

Statistical analysis

Data were presented as the mean ± standard deviation and analyzed using GraphPad Prism 9 software. The experiment was performed at least three times to ensure reproducibility of the results. Normality of all experimental data was verified by the Shapiro–Wilk test, and in the case that all data conformed to normal distribution, one-way analysis of variance (ANOVA) was used to evaluate the differences between groups. The Student–Newman–Keuls test was utilized to examine the differences between each pair of groups. Statistical significance was determined at a p-value of less than 0.05.

Results

Synthesis and characterization of Ti$_3$C$_2$–PVP nanosheets

As shown in Fig. 1A, the Ti$_3$C$_2$ MXene nanosheets were synthesized through a process involving the etching of the precursor Ti$_3$AlC$_2$ MAX. To enhance the stability of Ti$_3$C$_2$ nanosheets, surface modification was carried out utilizing PVP. The morphology of Ti$_3$C$_2$ nanosheets was characterized by SEM and TEM. As shown in Fig. 1B and C, the SEM and TEM images revealed that the exfoliated Ti$_3$C$_2$ nanosheets were well-layered and exhibited a typical two-dimensional layered structure with a lateral size of several hundred nanometers. To confirm the complete etching of the Al atomic layer, XRD was performed to analyze the crystal structure of the Ti$_3$C$_2$ MXene. The XRD pattern (Fig. 1D) showed that all the characteristic peaks of Ti$_3$AlC$_2$ had weakened or disappeared, except for the (002) peak which shifted to the lower angle, indicating the successful synthesis of Ti$_3$C$_2$ MXene and the complete etching of the Al atomic layer.

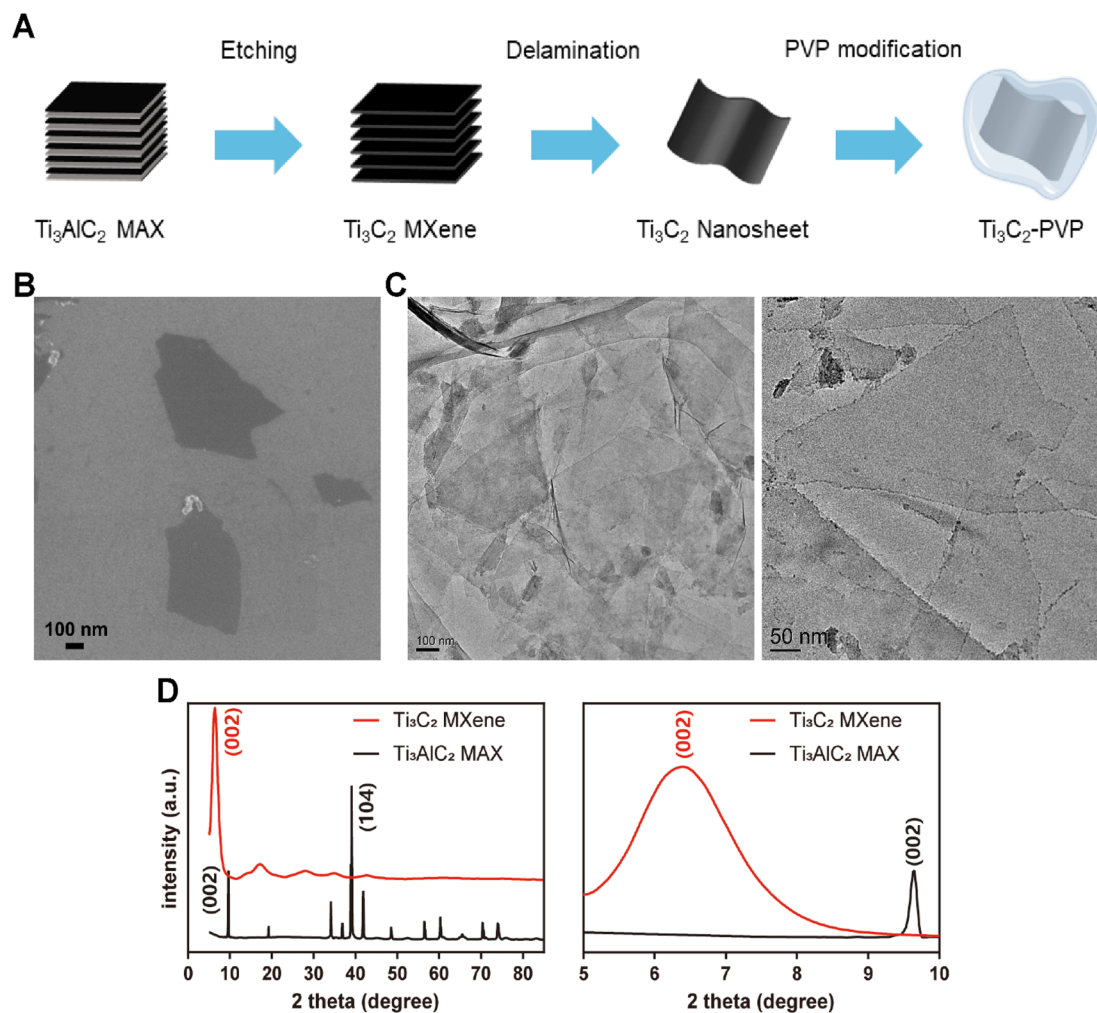Fig. 1 Characterization. (A) Schematic of the preparation of Ti_3C_2 MXene nanosheets and PVP modification. (B) SEM image of Ti_3C_2 nanosheets. (C) TEM images of Ti_3C_2 nanosheets. (D) XRD pattern of Ti_3AlC_2 MAX and Ti_3C_2 MXene.

Although Ti_3C_2 nanosheets exhibited good dispersion and stability in water, the poor stability in saline solution (PBS) and Dulbecco's modified Eagle medium (DMEM) resulted in significant agglomeration as illustrated in Fig. 2A. The modified Ti_3C_2 nanosheets (Ti_3C_2–PVP) exhibited improved dispersion and colloidal stability in a variety of simulated physiological media, including water, PBS, and DMEM. The UV-vis-NIR absorption spectra were analyzed to determine the effect of PVP modification on the optical properties of Ti_3C_2 nanosheets. The results, as shown in Fig. 2B, indicated that the PVP modification did not have a negative effect on the optical properties of Ti_3C_2 nanosheets, as evidenced by the absorption peak near 800 nm of Ti_3C_2–PVP. The absorption peak of Ti_3C_2–PVP was located in the NIR region, highlighting the potential of the nanosheet to absorb 808 nm NIR light.

In order to determine the effectiveness of the surface modification of Ti_3C_2–PVP nanosheets, zeta potential analysis was performed. The results (Fig. 2C) showed that the Ti_3C_2 nanosheets were stable in deionized water and had a zeta potential of -23.33 ± 0.81 mV. After modification with PVP, the zeta potential decreased to -4.717 ± 0.63 mV, indicating that

the macromolecular chains of PVP form a layer of spatial resistance on the surface of the Ti_3C_2 nanosheets. To further evaluate the colloidal stability of Ti_3C_2–PVP nanosheets in physiological solutions, dynamic light scattering (DLS) was performed to determine the hydrodynamic size distribution. The results (Fig. 2D–F) showed that the hydrodynamic size of Ti_3C_2 in water, PBS, and DMEM was 611.0 ± 2.718 nm, 554.2 ± 27.53 nm, and 695.2 ± 13.69 nm, respectively. In contrast, Ti_3C_2–PVP in water, PBS, and DMEM showed smaller nanosheet sizes, which were 351.6 ± 6.313 nm, 412.9 ± 6.350 nm, and 266.7 ± 2.483 nm, respectively.

Photothermal property of Ti_3C_2–PVP nanosheets

The photothermal heating ability was investigated by measuring the temperature of Ti_3C_2 and Ti_3C_2–PVP nanosheets of different concentrations (100, 50, 25, and 12.5 $\mu g\ mL^{-1}$) after exposure to 808 nm NIR laser at a power density of 1.0 W cm^{-2}. As depicted in Fig. 3A and B, the results showed that both Ti_3C_2 and Ti_3C_2–PVP colloidal solution achieved a temperature increase to 65 °C (100 $\mu g\ mL^{-1}$) and 40 °C (12.5 $\mu g\ mL^{-1}$), respectively, within 3 minutes of NIR laser exposure. At
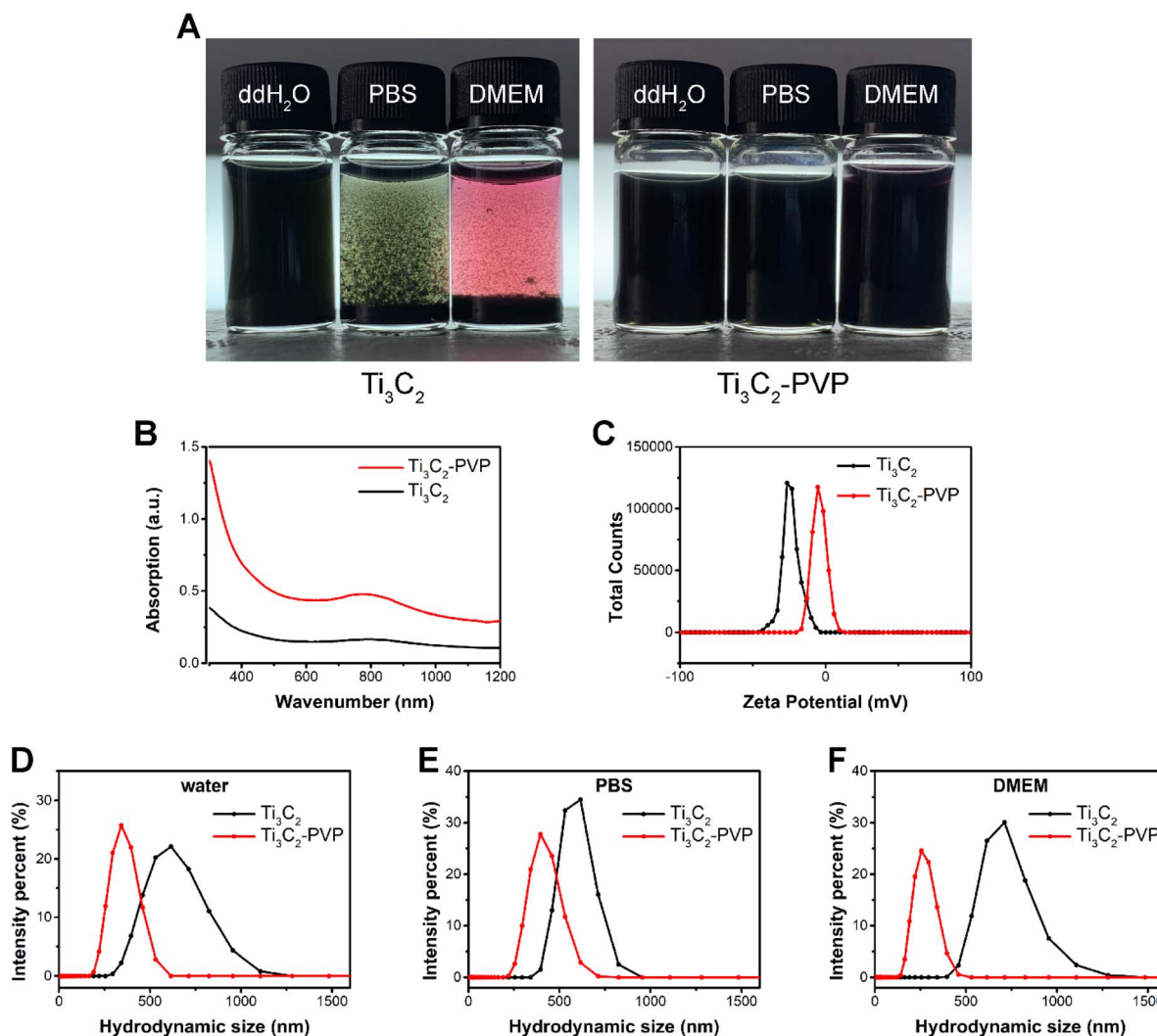
Fig. 2 Stability of Ti_3C_2–PVP nanosheets. (A) Photographs of Ti_3C_2 and Ti_3C_2–PVP nanosheets in water, PBS, and media (DMEM) at least 1 week. (B) UV-vis-NIR absorption spectra of Ti_3C_2 and Ti_3C_2–PVP. (C) Zeta potential analysis of Ti_3C_2 and Ti_3C_2–PVP in water. (D–F) Hydrodynamic size of Ti_3C_2 and Ti_3C_2–PVP in water, PBS, and media (DMEM).

concentrations of 50 μg mL^{-1} and 25 μg mL^{-1}, the temperature of Ti_3C_2–PVP nanosheets decreased slightly to 57.5 and 47.1 °C, respectively, compared to 63.7 and 50.5 °C of Ti_3C_2 nanosheets.

Furthermore, the photothermal performance of Ti_3C_2–PVP nanosheets (12.5 μg mL^{-1}) was evaluated at different NIR power densities. The results, shown in Fig. 3C, indicated that after 3 minutes of exposure to NIR light at a power density of 1.0 W cm^{-2}, the temperature of Ti_3C_2–PVP increased by 15.6 °C, which was comparable to the temperature increase of 16.7 °C for Ti_3C_2. In addition, at a power density of 0.5 W cm^{-2}, the temperature of Ti_3C_2–PVP increased by 3.7 °C, while the temperature of Ti_3C_2 increased by 4.2 °C.

To evaluate the photothermal stability of Ti_3C_2–PVP nanosheets, we evaluated the temperature change during five consecutive ON/OFF cycles of the NIR laser. The results (Fig. 3D) indicated that Ti_3C_2–PVP nanosheets colloidal solution showed no decrease in temperature during the ON/OFF cycles, indicating their good photothermal stability and suitability for

repeated and effective use in photothermal treatment processes.

Biocompatibility analysis

In order to evaluate the biocompatibility of Ti_3C_2–PVP nanosheets, the effect on the cell proliferation ability of BMSCs was analyzed using the CCK-8 assay. The BMSCs were co-cultured with Ti_3C_2–PVP nanosheets for 1, 3, 5, and 7 days, and the results (Fig. 4A) showed that Ti_3C_2–PVP exhibited good biocompatibility at low concentrations (12.5 and 25 μg mL^{-1}). However, at a concentration of 50 μg mL^{-1}, a significant inhibition of cell proliferation was observed at 1 day. Notably, at a concentration of 12.5 μg mL^{-1}, Ti_3C_2–PVP nanosheets significantly promoted cell proliferation at 5 days. Considering the biocompatibility and photothermal properties, the concentration of 12.5 μg mL^{-1} of Ti_3C_2–PVP nanosheets colloidal solution was selected for subsequent experiments.
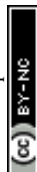
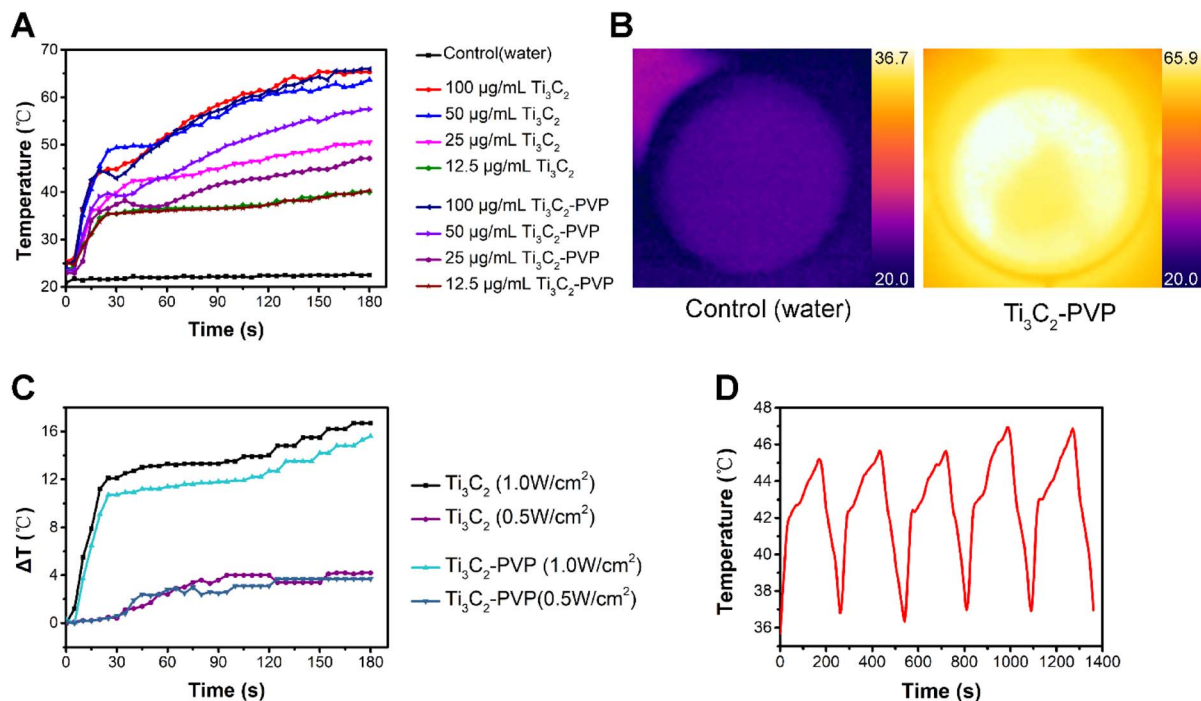Fig. 3 Photothermal properties of Ti_3C_2–PVP nanosheets. (A) Photothermal heating curves of Ti_3C_2 and Ti_3C_2–PVP colloidal solution with different concentrations (100, 50, 25, 12.5 μg mL^{-1}) under 808 nm NIR irradiation (1.0 W cm^{-2}). (B) Infrared thermal images of water and Ti_3C_2–PVP colloidal solutions (100 μg mL^{-1}) under 808 nm laser irradiation (1.0 W cm^{-2}). (C) Temperature change curves of Ti_3C_2–PVP colloidal solutions (12.5 μg mL^{-1}) under 808 nm NIR irradiation at different power densities (0.5, 1.0 W cm^{-2}). (D) Recycling heating curves of Ti_3C_2–PVP colloidal solutions (12.5 μg mL^{-1}) for five ON/OFF cycles under 808 nm NIR laser (1.0 W cm^{-2}).

The effect of the photothermal effect of Ti_3C_2–PVP nanosheets on cell viability and proliferation was further evaluated by CCK-8 and live/dead staining. The CCK-8 results, as shown in Fig. 4B, indicated that cell proliferation was significantly enhanced at 1 day in the Ti_3C_2–PVP + NIR group, but no significant difference was observed at 3, 5, and 7 days, when compared with the other groups. Live/dead staining, as shown in Fig. 4C, revealed that all groups showed strong green fluorescence, indicating that most of the cells were viable and only a small number of cells were dead (red fluorescence).

Cellular interactions of Ti_3C_2–PVP nanosheets with BMSCs

Bright field imaging and SEM were used to determine the interaction of Ti_3C_2–PVP nanosheets with BMSCs. As illustrated in Fig. 5A, after co-culture with Ti_3C_2–PVP for 24 hours, the cells appeared to be heavily enriched with nanosheets, as indicated by the black sheet-like material present on the cell surface.

The SEM results (Fig. 5B) confirmed that Ti_3C_2–PVP nanosheets tended to bind to the cell membrane, showing significant enrichment compared to the cell culture substrate. The effect of photothermal treatment on the morphology of BMSCs was also examined by staining for cytoskeletal actin. The results, as shown in Fig. 5C, showed that BMSCs in the Ti_3C_2–PVP + NIR group exhibited a flatter shape and larger spreading area compared to the other groups, suggesting that photothermal treatment promoted the adhesion of BMSCs.

Photothermal osteogenic effect of Ti_3C_2–PVP nanosheets on BMSCs

To evaluate the photothermal modulation of Ti_3C_2–PVP on the osteogenic differentiation of BMSCs, the relative mRNA expression levels of osteogenic markers, including ALP, OCN, OPN, RUNX2, and COL1, were evaluated by qRT-PCR after 14 days of osteogenic induction. The results (Fig. 6A–E) showed that the expression levels of ALP, OCN, OPN, RUNX2, and COL1 were significantly increased in the Ti_3C_2–PVP + NIR group compared with the other groups. Conversely, NIR irradiation alone without Ti_3C_2–PVP did not affect gene expression. In addition, the expression levels of ALP, OCN, RUNX2, and COL1 were also significantly higher in the Ti_3C_2–PVP group than in the control group. The findings of the photothermal modulation of osteogenic differentiation were further confirmed by ALP staining (Fig. 7A and B) and alizarin red staining (Fig. 7C and D). After 7 and 14 days of osteogenic induction, the group treated with Ti_3C_2–PVP and NIR showed the highest levels of ALP activity and the number of calcium salt deposits. Furthermore, the ALP activity and mineralization were also significantly higher in the Ti_3C_2–PVP group compared with the control group.

Discussion

Two-dimensional nanomaterials and their derivatives have been extensively studied for their potential to regulate stem cell behavior in tissue regeneration.[21] Graphene has been widely
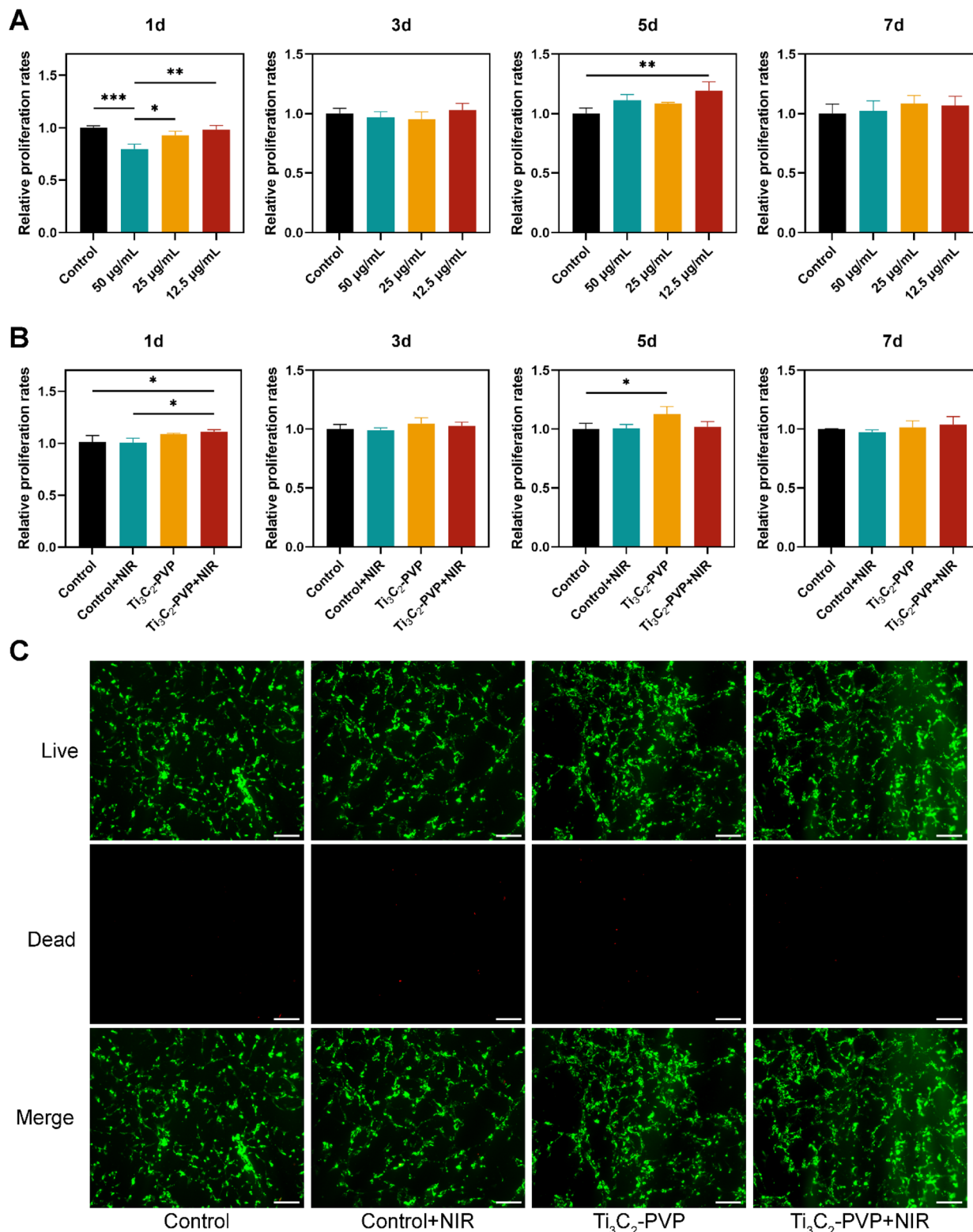
Fig. 4 Biocompatibility assessments. (A) Relative proliferation rates of BMSCs cells co-cultured with Ti_3C_2–PVP nanosheets at concentrations of 50, 25, 12.5, 0 μg mL^{-1} for 1, 3, 5 and 7 days. ($n = 3$, $*p < 0.05$, $**p < 0.01$, $***p < 0.001$). (B) Relative proliferation rates of BMSCs co-cultured with growth medium and Ti_3C_2–PVP nanosheets at concentrations of 12.5 μg mL^{-1} with or without NIR irradiation for 1, 3, 5 and 7 days ($*p < 0.05$). (C) Live/dead double staining, cells co-cultured with Ti_3C_2–PVP nanosheets with or without NIR irradiation for 24 h. Red staining represents dead cells while green fluorescence indicates live cells. Scale bars: 200 μm.
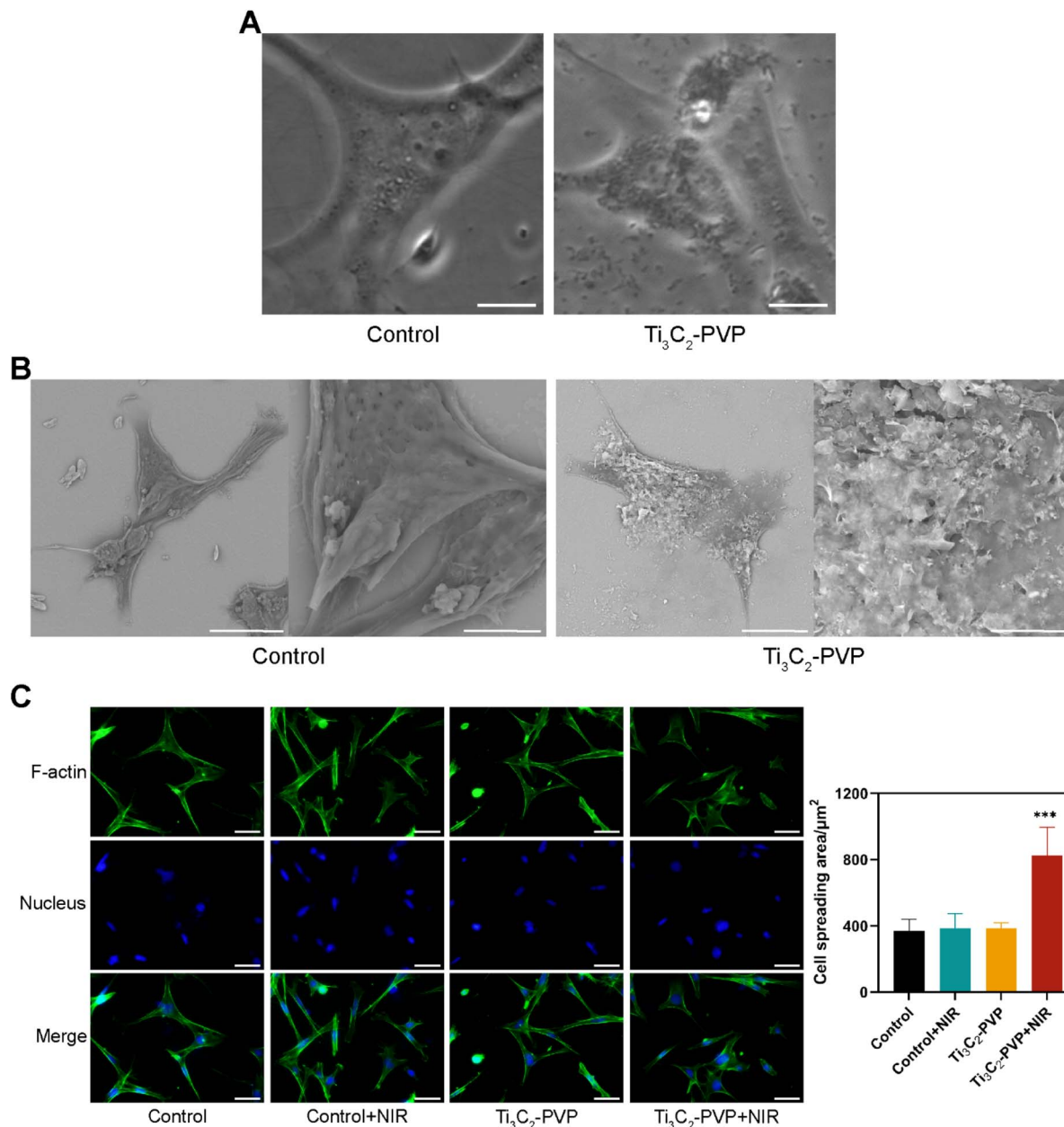
Fig. 5 Cellular interactions of Ti_3C_2–PVP nanosheets with BMSCs. (A) Bright field imaging of BMSCs co-cultured with Ti_3C_2–PVP. Scale bars: 10 μm. (B) SEM images of BMSCs co-cultured with Ti_3C_2–PVP. Scale bars: 30 μm (left), 8 μm (right). (C) Cytoskeleton immunofluorescence image of BMSCs co-cultured with Ti_3C_2–PVP with or without NIR irradiation and quantitative data of cell spreading area ($n = 3$, ***$p < 0.001$, comparison between control and other groups). Scale bars: 50 μm.

regarded as a promising biocompatible scaffold for promoting the proliferation of mesenchymal stem cells and accelerating their differentiation into osteoblasts.[30] MXenes, a family of two-dimensional materials consisting of transition metal carbides and nitrides, have been increasingly studied for their effects on stem cells.[24] Despite the growing interest in the modulation of MXenes on stem cells, no studies have been reported on their photothermal modulation. Further research on the photothermal modulation of MXenes on stem cells would contribute to the advancement of MXene applications and photothermal therapy in regenerative medicine and tissue engineering.

Firstly, we successfully synthesized Ti_3C_2 MXene nanosheets using a method reported in the literature.[29] The morphology of Ti_3C_2 MXene was confirmed by SEM and TEM imaging, which showed the typical two-dimensional structure of these materials. The XRD pattern was consistent with previous literature reports and indicated that the Ti_3C_2 MXene was successfully synthesized through chemical etching without any residue of the precursor Ti_3AlC_2.[29] The results of UV-vis-NIR spectra analysis indicated that the modified Ti_3C_2–PVP nanosheets retained a strong NIR absorption capability, with a characteristic peak at 800 nm, which falls within the biological NIR window (650–950
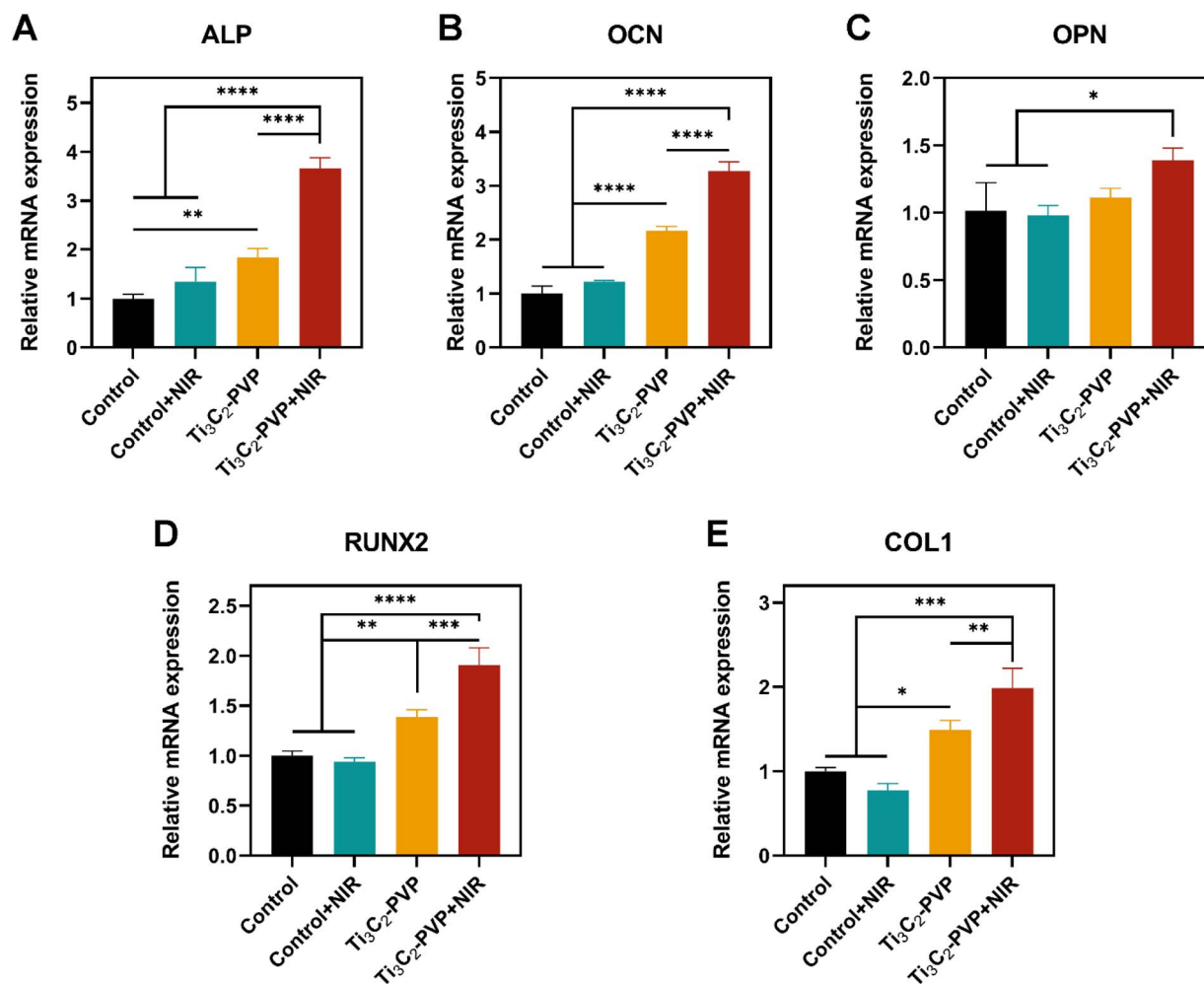
Fig. 6 mRNA levels of the osteogenic differentiation-related genes ALP (A), OCN (B), OPN (C), RUNX2 (D) and COL1 (E) in BMSCs co-cultured with Ti_3C_2–PVP nanosheets with or without NIR irradiation ($n = 3$, $*p < 0.05$, $**p < 0.01$, $***p < 0.001$, $****p < 0.0001$).

nm).[31] The stability of Ti_3C_2 MXene nanosheets in physiological solutions is a critical issue due to their aggregation in salt solutions and susceptibility to oxidation.[25,26] This instability can negatively affect the material's biocompatibility and limit its practical use in the field of medicine. To address this issue, we used PVP as a surface modifier to improve the stability of the Ti_3C_2 nanosheets. The visual observations and DLS assays showed that the addition of PVP significantly improved the colloidal stability of the Ti_3C_2–PVP nanosheets in water, PBS, and DMEM solutions. The improved stability of the Ti_3C_2 MXene nanosheets in physiological solutions can be attributed to the presence of the organic chain of PVP. This organic chain reduces the strong interaction between the surface of the nanomaterial and biomolecules or ions, thereby providing a protective layer.[32] This protective layer helps to maintain the stability of the nanomaterial in complex physiological environments, making it more suitable for biomedical applications.

Secondly, it was observed that the surface modification of Ti_3C_2–PVP nanosheets did not compromise their photothermal properties, as evidenced by the temperature increase induced by NIR irradiation of the Ti_3C_2–PVP colloidal solutions. Even at

a low NIR power of 0.5 W cm^{-2} and a low concentration of 12.5 µg mL^{-1}, the colloidal solutions of Ti_3C_2–PVP nanosheets were able to induce a temperature increase of 3.7 °C. In contrast to photothermal therapy for antitumor and antimicrobial purposes, which often require higher temperatures, photothermal therapy for tissue regeneration is limited to lower temperatures to minimize tissue damage, typically a temperature increase of only 3–5 °C above the body temperature.[10,12–14] Therefore, the photothermal properties of Ti_3C_2–PVP nanosheets are well-suited for applications in regenerative medicine.

Thirdly, we found that the cytocompatibility of Ti_3C_2–PVP nanosheets is concentration-dependent. While high concentrations (50 µg mL^{-1}) were observed to inhibit cell proliferation, low concentrations (12.5 µg mL^{-1}) were found to promote cell proliferation. Notably, we found that high concentrations of Ti_3C_2–PVP nanosheets exhibited cytotoxicity only on the first day but did not inhibit cell proliferation at subsequent time points (3, 5, and 7 days). The biocompatibility of MXene materials is still under debate, with some studies suggesting that MXene is negligible at cytotoxic concentrations of up to 500 mg L^{-1},[33] while others have reported a decrease in cell
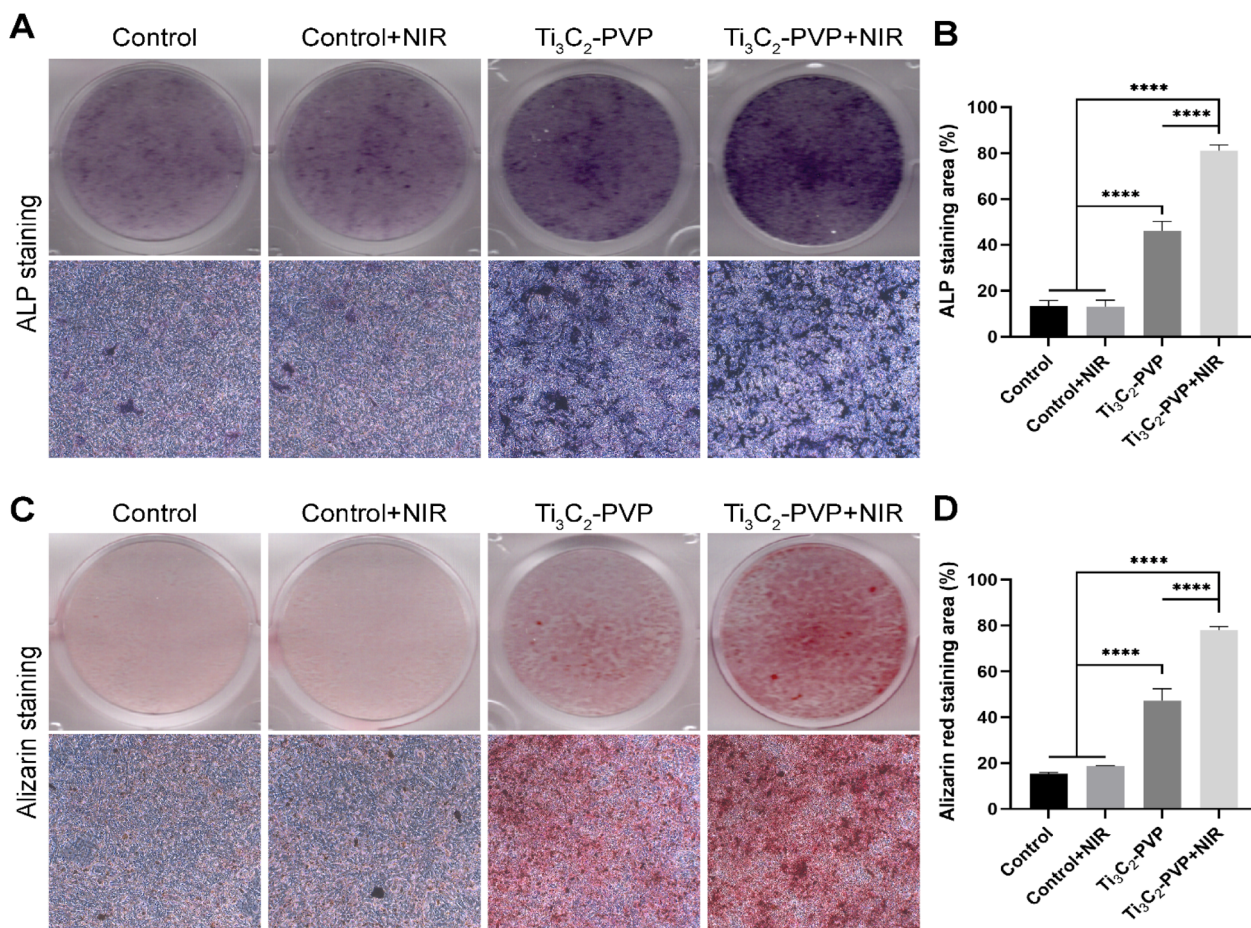
Fig. 7 Ti$_3$C$_2$–PVP nanosheets and photothermal treatment promote the osteogenesis of BMSCs. (A and C) The ALP staining and the alizarin staining of BMSCs co-cultured with Ti$_3$C$_2$–PVP with or without NIR irradiation. (B and D) Corresponding quantitative data of ALP and alizarin staining ($n = 3$, ****$p < 0.0001$).

viability at a concentration of 1.5 μg mL^{-1}.[34] Our results showed that Ti$_3$C$_2$–PVP tended to accumulate on the cell membrane rather than on the substrate of 2D cell cultures, which may also contribute to cytotoxicity at high concentrations. Thus, from our perspective, Ti$_3$C$_2$–PVP nanosheets have good biocompatibility for tissue engineering applications.

Based on previous studies,[35–37] we targeted a temperature of 42 °C for photothermal osteogenesis. The temperature of the co-cultures of BMSCs and Ti$_3$C$_2$–PVP was regulated by adjusting the NIR power and monitored with an infrared imager. Our results showed that the photothermal treatment promoted cell proliferation in the early stages. Similar results have been reported in the literature, where photothermal treatment at 40–43 °C promoted the proliferation of preosteoblasts at 24 and 48 h.[13] In addition, we observed that cells exposed to Ti$_3$C$_2$–PVP and NIR exhibited a flatter morphology, better spreading and osteoblastic morphology. This observation is in consistent with previous reports, indicating that wider cell spreading and formation of many filopodia can promote osteogenic differentiation of stem cells.[38]

Fourthly, to evaluate the osteogenic potential of Ti$_3$C$_2$–PVP nanosheets, we utilized qRT-PCR, ALP staining, and ARS staining techniques to measure the expression of osteogenesis-related genes, including ALP, OCN, OPN, RUNX2, and COL1,[39] as well as the ALP activity and mineralization of BMSCs. Our results showed that Ti$_3$C$_2$–PVP significantly promoted the osteogenic differentiation of BMSCs. These findings are consistent with several recent studies that have confirmed the good osteogenic activity of Ti$_3$C$_2$ MXene.[40–46] The mechanism by which Ti$_3$C$_2$ MXene promotes osteogenic differentiation of MSCs may involve the activation of the Wnt/β-catenin signaling pathway.[24]

Next, our study presented novel insights into the modulation of osteogenic differentiation of BMSCs through photothermal conversion. We found that the photothermal effect of Ti$_3$C$_2$–PVP under NIR light further promoted the mRNA expression of osteogenic markers, ALP activity, and mineralization of BMSCs. Gentle photothermal stimulation has been widely demonstrated to promote osteogenesis.[47–49] Heat shock protein (HSP) plays a key role in the regulation of photothermal osteogenesis.[13,35,50] HSPs are a group of highly conserved molecular

chaperones whose expression is generally increased in response to high temperature or other physicochemical stimuli.[51] In recent years, studies have reported an important role of HSPs in bone metabolism.[52,53] Thermal stimulation upregulates HSP expression and promotes osteogenesis through several signaling pathways, including ERK, Wnt/β-catenin, MAPK, and PI3K-Akt.[50,54]

In the field of photothermal treatment, the parameters used for tissue regeneration can vary. Previous studies have employed different times of NIR irradiation, ranging from longer periods of approximately 1 hour to shorter periods of approximately 60 seconds.[35,50] In our study, we selected a 5 minute daily irradiation frequency, based on previous reports. During the 14 day experiment, the viability of BMSCs was maintained, indicating the safety of our photothermal treatment.

The study revealed that the photothermal effect of Ti_3C_2 represents a promising and emerging strategy in tissue engineering, though certain limitations exist in the current investigation. Specifically, in the absence of inorganic or polymer scaffold materials, Ti_3C_2–PVP nanosheets are susceptible to metabolic degradation by the body fluid environment, resulting in an unstable delivery of photothermal stimulation in the bone defect area when used alone. Therefore, limited by the physical properties of Ti_3C_2–PVP nanosheets, this study only explored their photothermal regulation of BMSCs, and animal experiments to investigate the pro-osteogenic efficiency of Ti_3C_2–PVP nanosheets *in vivo* were not conducted. Consequently, in future research, we plan to fabricate degradable composite films or implants by incorporating Ti_3C_2–PVP with biocompatible polymer materials. This will enable us to investigate the *in vivo* application strategies of Ti_3C_2–PVP and its photothermal modulation capability.

Conclusions

In this study, surface modification of Ti_3C_2 MXene nanosheets with PVP (Ti_3C_2–PVP) was employed to enhance their colloidal stability in physiological solutions. Ti_3C_2 nanosheets were found to exhibit good biocompatibility and desirable photothermal properties, making them a promising candidate for regenerative medicine applications. The possibility of using thermal stimulation instead of growth factors in bone tissue engineering was explored by co-culturing Ti_3C_2–PVP nanosheets with BMSCs and irradiating with 808 nm NIR. Our results showed that the photothermal stimulation generated by Ti_3C_2–PVP nanosheets was able to promote cell proliferation, adhesion, and osteogenic differentiation of BMSCs. In conclusion, photothermal conversion of Ti_3C_2–PVP nanosheets can modulate the cellular functions of BMSCs and has potential for bone tissue engineering applications.

Author contributions

Jiebing Zhang: conceptualization, data curation, investigation, methodology, visualization, writing – original draft. Shuang Tang: data curation, formal analysis. Ning Ding: methodology.

Ping Ma: resources, software. Zutai Zhang: conceptualization, funding acquisition, writing – review & editing. Project administration.

Conflicts of interest

There are no conflicts to declare.

Acknowledgements

References

1 R. T. Annamalai, X. Hong, N. G. Schott, G. Tiruchinapally, B. Levi and J. P. Stegemann, *Biomaterials*, 2019, **208**, 32–44.

2 C. J. Norris, G. J. Meadway, M. J. O'Sullivan, I. P. Bond and R. S. Trask, *Adv. Funct. Mater.*, 2011, **21**, 3624–3633.

3 G. Zhu, T. Zhang, M. Chen, K. Yao, X. Huang, B. Zhang, Y. Li, J. Liu, Y. Wang and Z. Zhao, *Bioact. Mater.*, 2021, **6**, 4110–4140.

4 X. Hu, Y. Wang, Y. Tan, J. Wang, H. Liu, Y. Wang, S. Yang, M. Shi, S. Zhao, Y. Zhang and Q. Yuan, *Adv. Mater.*, 2017, **29**, 1605235.

5 T. Yin and L. Li, *J. Clin. Investig.*, 2006, **116**, 1195–1201.

6 T. J. Blokhuis and J. J. Arts, *Injury*, 2011, **42**(suppl. 2), S26–S29.

7 H. S. Azevedo and I. Pashkuleva, *Adv. Drug Deliv. Rev.*, 2015, **94**, 63–76.

8 C. J. Kowalczewski and J. M. Saul, *Front. Pharmacol.*, 2018, **9**, 513.

9 H. A. Rather, D. Jhala and R. Vasita, *Mater. Sci. Eng., C*, 2019, **103**, 109761.

10 Y. Kong, J. Duan, F. Liu, L. Han, G. Li, C. Sun, Y. Sang, S. Wang, F. Yi and H. Liu, *Chem. Soc. Rev.*, 2021, **50**, 12828–12872.

11 A. J. McGrath, Y. H. Chien, S. Cheong, D. A. Herman, J. Watt, A. M. Henning, L. Gloag, C. S. Yeh and R. D. Tilley, *ACS Nano*, 2015, **9**, 12283–12291.

12 S. Sayed, O. Faruq, M. Hossain, S. B. Im, Y. S. Kim and B. T. Lee, *Mater. Sci. Eng., C*, 2019, **105**, 110027.

13 X. Zhang, G. Cheng, X. Xing, J. Liu, Y. Cheng, T. Ye, Q. Wang, X. Xiao, Z. Li and H. Deng, *J. Phys. Chem. Lett.*, 2019, **10**, 4185–4191.

14 R. Nørgaard, M. Kassem and S. I. Rattan, *Ann. N. Y. Acad. Sci.*, 2006, **1067**, 443–447.

15 S. K. Sharma, N. Shrivastava, F. Rossi, L. D. Tung and N. T. K. Thanh, *Nano Today*, 2019, **29**, 100795.

16 R. Kurapati, K. Kostarelos, M. Prato and A. Bianco, *Adv. Mater.*, 2016, **28**, 6052–6074.

17 K. Yang, S. Zhang, G. Zhang, X. Sun, S.-T. Lee and Z. Liu, *Nano Lett.*, 2010, **10**, 3318–3323.

18 J. R. Melamed, R. S. Edelstein and E. S. Day, *ACS Nano*, 2015, **9**, 6–11.

19 J.-W. Xu, K. Yao and Z.-K. Xu, *Nanoscale*, 2019, **11**, 8680–8691.

20 S. A. Leon, S. O. Asbell, H. H. Arastu, G. Edelstein, A. J. Packel, S. Sheehan, I. Daskal, G. G. Guttmann and I. Santos, *Int. J. Hyperthermia*, 1993, **9**, 77–87.

21 A. Murali, G. Lokhande, K. A. Deo, A. Brokesh and A. K. Gaharwar, *Mater. Today*, 2021, **50**, 276–302.

22 J. Xuan, Z. Wang, Y. Chen, D. Liang, L. Cheng, X. Yang, Z. Liu, R. Ma, T. Sasaki and F. Geng, *Angew. Chem., Int. Ed.*, 2016, **55**, 14569–14574.

23 K. Huang, Z. Li, J. Lin, G. Han and P. Huang, *Chem. Soc. Rev.*, 2018, **47**, 5109–5124.

24 D. Cui, N. Kong, L. Ding, Y. Guo, W. Yang and F. Yan, *Adv. Healthc. Mater.*, 2021, **10**, e2101215.

25 H. Lin, X. Wang, L. Yu, Y. Chen and J. Shi, *Nano Lett.*, 2017, **17**, 384–391.

26 Y. Chae, S. J. Kim, S. Y. Cho, J. Choi, K. Maleski, B. J. Lee, H. T. Jung, Y. Gogotsi, Y. Lee and C. W. Ahn, *Nanoscale*, 2019, **11**, 8387–8393.

27 X. Liu, Y. Xu, Z. Wu and H. Chen, *Macromol. Biosci.*, 2013, **13**, 147–154.

28 L. E. Smith, S. Rimmer and S. MacNeil, *Biomaterials*, 2006, **27**, 2806–2812.

29 M. Alhabeb, K. Maleski, B. Anasori, P. Lelyukh, L. Clark, S. Sin and Y. Gogotsi, *Chem. Mater.*, 2017, **29**, 7633–7644.

30 T. R. Nayak, H. Andersen, V. S. Makam, C. Khaw, S. Bae, X. Xu, P. L. Ee, J. H. Ahn, B. H. Hong, G. Pastorin and B. Özyilmaz, *ACS Nano*, 2011, **5**, 4670–4678.

31 M. F. Tsai, S. H. Chang, F. Y. Cheng, V. Shanmugam, Y. S. Cheng, C. H. Su and C. S. Yeh, *ACS Nano*, 2013, **7**, 5330–5342.

32 K. M. Koczkur, S. Mourdikoudis, L. Polavarapu and S. E. Skrabalak, *Dalton Trans.*, 2015, **44**, 17883–17905.

33 D. Zhang, W. Zheng, X. Li, A. Li, N. Ye, L. Zhang, Y. Liu, X. Liu, R. Zhang, M. Wang, J. Cheng, H. Yang and M. Gong, *Carbon*, 2021, **178**, 810–821.

34 S. Kyrylenko, O. Gogotsi, I. Baginskiy, V. Balitskyi, V. Zahorodna, Y. Husak, I. Yanko, M. Pernakov, A. Roshchupkin, M. Lyndin, B. B. Singer, V. Buranych, A. Pogrebnjak, O. Sulaieva, O. Solodovnyk, Y. Gogotsi and M. Pogorielov, *ACS Appl. Mater. Interfaces*, 2022, **14**, 28683–28696.

35 L. Tong, Q. Liao, Y. Zhao, H. Huang, A. Gao, W. Zhang, X. Gao, W. Wei, M. Guan, P. K. Chu and H. Wang, *Biomaterials*, 2019, **193**, 1–11.

36 J. Chen, Z. D. Shi, X. Ji, J. Morales, J. Zhang, N. Kaur and S. Wang, *Tissue Eng., Part A*, 2013, **19**, 716–728.

37 C. P. Ye, B. C. Heng, H. Liu, W. S. Toh and T. Cao, *Cell Biochem. Funct.*, 2007, **25**, 267–276.

38 R. Peng, X. Yao, B. Cao, J. Tang and J. Ding, *Biomaterials*, 2012, **33**, 6008–6019.

39 S. Khoshniat, A. Bourgine, M. Julien, M. Petit, P. Pilet, T. Rouillon, M. Masson, M. Gatius, P. Weiss, J. Guicheux and L. Beck, *Bone*, 2011, **48**, 894–902.

40 R. Huang, X. Chen, Y. Dong, X. Zhang, Y. Wei, Z. Yang, W. Li, Y. Guo, J. Liu, Z. Yang, H. Wang and L. Jin, *ACS Appl. Bio Mater.*, 2020, **3**, 2125–2131.

41 X. Mi, Z. Su, Y. Fu, S. Li and A. Mo, *Biomed. Mater.*, 2022, **17**, 035002.

42 Y. Fu, J. Zhang, H. Lin and A. Mo, *Mater. Sci. Eng., C*, 2021, **118**, 111367.

43 K. Chen, Y. Chen, Q. Deng, S.-H. Jeong, T.-S. Jang, S. Du, H.-E. Kim, Q. Huang and C.-M. Han, *Mater. Lett.*, 2018, **229**, 114–117.

44 Y. Fu, S. Huang, Z. Feng, L. Huang, X. Zhang, H. Lin and A. Mo, *ACS Biomater. Sci. Eng.*, 2023, **9**, 900–917.

45 S. Pan, J. Yin, L. Yu, C. Zhang, Y. Zhu, Y. Gao and Y. Chen, *Adv. Sci.*, 2020, **7**, 1901511.

46 S. H. Lee, S. Jeon, X. Qu, M. S. Kang, J. H. Lee, D.-W. Han and S. W. Hong, *Nano Converg.*, 2022, **9**, 38.

47 Y. Zhao, X. Peng, D. Wang, H. Zhang, Q. Xin, M. Wu, X. Xu, F. Sun, Z. Xing, L. Wang, P. Yu, J. Xie, J. Li, H. Tan, C. Ding and J. Li, *Adv. Sci.*, 2022, **9**, 2204535.

48 Y. Wu, Q. Liao, L. Wu, Y. Luo, W. Zhang, M. Guan, H. Pan, L. Tong, P. K. Chu and H. Wang, *ACS Nano*, 2021, **15**, 17854–17869.

49 Q. Fan, J. Bai, H. Shan, Z. Fei, H. Chen, J. Xu, Q. Ma, X. Zhou and C. Wang, *Bioact. Mater.*, 2021, **6**, 4014–4026.

50 H. Shan, X. Zhou, B. Tian, C. Zhou, X. Gao, C. Bai, B. Shan, Y. Zhang, S. Sun, D. Sun, Q. Fan, X. Zhou, C. Wang and J. Bai, *Biomaterials*, 2022, **284**, 121482.

51 P. G. Richardson, C. S. Mitsiades, J. P. Laubach, S. Lonial, A. A. Chanan-Khan and K. C. Anderson, *Br. J. Haematol.*, 2011, **152**, 367–379.

52 K. Hang, C. Ye, E. Chen, W. Zhang, D. Xue and Z. Pan, *Cell Stress Chaperones*, 2018, **23**, 1153–1164.

53 L. Li, L. Wang, Q. D. You and X. L. Xu, *J. Med. Chem.*, 2020, **63**, 1798–1822.

54 L. Tan, Y. Hu, M. Li, Y. Zhang, C. Xue, M. Chen, Z. Luo and K. Cai, *Chem. Eng. J.*, 2022, **431**, 133382.